An urban module coupled with the Variable Infiltration Capacity model to improve hydrothermal simulations in urban systems

Yibing Wang[1], Xianhong Xie[1*], Bowen Zhu[2], Arken Tursun[1], Fuxiao Jiang[3], Yao Liu[1], Dawei Peng[1], Buyun Zheng[1]

1. State Key Laboratory of Remote Sensing Science, Faculty of Geographical Science, Beijing Normal University, Beijing 100875, China
2. College of Water Science and Engineering, Taiyuan University of Technology, Taiyuan 030024, China
3. Institute of Earth Surface Dynamics, University of Lausanne, 1015 Lausanne, Switzerland

*Corresponding author:
        Xianhong Xie (Beijing Normal University, xianhong@bnu.edu.cn)

Abstract

Global urban expansion has altered surface aerodynamics and hydrothermal dynamics, aggravating environmental challenges such as urban heat/dry islands. To identify such environmental responses, various physical models, including urban canyon models (UCMs) and land surface models (LSMs), have been developed to represent surface hydrothermal processes. However, UCMs often treat a city as a unified entity and overlook subcity heterogeneity. LSMs are generally designed for natural land covers and lack the capability to capture urban characteristics. To address these limitations, the aim of this study is to couple an urban module with a sophisticated LSM, i.e., the Variable Infiltration Capacity (VIC) model. This coupled model, i.e., the VIC-urban model, is characterized by its ability to coordinate certain critical urban features, including the urban geometry, radiative interactions, and human impacts. Adopting Beijing as an evaluation site, the VIC-urban model shows higher performance than the original version, with excellent accuracy in simulating sensible heat, latent heat, runoff, and land surface temperature (LST). The absolute error is smaller than 25% for the sensible heat and latent heat, and smaller than 12% and 30% for the LST and runoff, respectively, which indicates that VIC-urban can effectively simulate hydrological and thermal fluxes in urban systems. Sensitivity analysis reveals that the roof emissivity and interception capacity exert the greatest impact on the roof temperature and evaporation, and the height-width ratio has the greatest influence on the canyon. Our work introduces a reliable option for large-scale land surface simulations that accounts for urban environments, and is among the first attempts to establish a systematic urban modelling framework of the VIC model. The VIC-urban model enables the analysis of urbanization-induced environmental changes and quantification of environmental variations among different urban configurations. The proposed model can thus offer invaluable insights for urban planners and landscape designers.

Key words: Urban canyon models; VIC model; Hydrothermal processes; Urban system; Sensitivity analysis

1. Introduction

Urban areas have been expanding globally and are characterized by increasing impervious surfaces and decreasing natural land coverage. This land cover change has led to alterations in surface aerodynamics and hydrothermal dynamics, resulting in decreased local evaporation and an exacerbation of temperature and extreme precipitation events (Yang et al., 2021). It has caused numerous environmental issues, such as urban heat islands (Morabito et al., 2021; Yao et al., 2021), urban dry islands (Meili et al., 2022; Li et al., 2021) and inundation problems (Mu et al., 2020; Huang et al., 2022). Moreover, cities encompass unique land surface processes, which differ from those of natural land surfaces. The difference results from the diverse urban configurations, varied building materials, and human interventions (Oh and Sushama, 2021). Therefore, it is necessary to accurately quantify the impacts of urbanization and develop proper mitigation strategies (Yao et al., 2021).

As efficient tools, various land surface models (LSMs) have been rapidly developed in recent decades, providing unprecedented opportunities to obtain detailed information on the storage and movement of surface energy and water cycles (Bierkens et al., 2015). LSMs have been used for various applications, such as land-climate interactions (Zhong et al., 2020; Wang et al., 2020), hydrothermal environment quantifications (Zhao et al., 2019; Huang et al., 2022), and dataset productions (Hersbach et al., 2020; Rodell et al., 2004). However, LSMs are generally formulated for natural land surfaces (Best and Grimmond, 2015), and often overlook the unique characteristics (e.g., urban configurations and buildings) of urban systems. Specific models should be developed or improved by considering the complexity and uniqueness within cities.

The existing urban parameterization schemes in LSMs mainly involve the bulk approach and coupling with urban canopy models (UCMs) (Ji et al., 2021; Meng, 2015). The bulk approach treats

urban surfaces as a regular land cover category with modified thermal and hydrological parameters (e.g.,

albedo and infiltration) (Wang et al., 2020; Yang et al., 2010), but still lacks consideration of urban-

specific characteristics, such as building blocking, radiative interactions (Salvadore et al., 2015),

artificial heating and irrigation (Chen et al., 2022). Coupling LSMs with UCMs (hereafter referred to as

LSM-UCMs) is also a popular strategy for capturing land surface processes in urban systems. Various

LSM-UCMs have been favorably applied in studies (Meng, 2015; Mcnorton et al., 2021; Yang et al.,

2010), including the Met Office–Reading Urban Surface Exchange Scheme (MORUSES) (Simón-

Moral et al., 2019), Community Land Model-Urban (CLMU) (Oleson and Feddema, 2020), and

Geophysical Fluid Dynamics Laboratory land model LM3 (LM3-UCM) (Li et al., 2016a). However,

there remains a shortage of LSM-UCM models, typically oversimplifying the dynamics of land cover

and climate change by using constant parameters in simulations (Kusaka et al., 2001).

To better represent urban environments, more suitable methodologies are needed (Yao et al., 2021).

Among the various LSM models, the Variable Infiltration Capacity (VIC) model is widely used for

identifying thermal and hydrological processes on land surfaces (Meng et al., 2019; Meng et al., 2020;

Zhu et al., 2020). VIC is characterized by grid-independent calculation and favorable consideration of

multiple layers along both horizontal (i.e., land cover types) and vertical (i.e., soil layers) directions

(Liang and Xie, 2001; Liang et al., 1996). The model can be coupled with multiple remote sensing data

(e.g., shortwave/longwave radiation, albedo, and leaf area index [LAI]) (Jiang et al., 2022; Meng et al.,

2020; Wang et al., 2022), to consider the realistic dynamics in land surface properties and atmospheric

conditions. The VIC model has been implemented in several urban-related studies based on the bulk

approach, and has provided an acceptable performance in simulating energy and hydrological fluxes

(Yang et al., 2010; Mishra et al., 2010; Wang et al., 2020). Yet a systematic urban calculation method

84   that considers the unique urban characteristics within VIC is still lacking.

85   In this study, we developed an urban module within the VIC model based on the Urban Tethys-

86   Chloris model (UT&C) (Meili et al., 2020), namely, the VIC-urban model. The coupled model can

87   efficiently identify urban hydrothermal processes when solving the water and energy balance and

88   consider unique urban characteristics, including urban geometry, radiative interactions among urban

89   surfaces (i.e., roof, canyon, walls, and ground), and human interference (e.g., irrigation and indoor

90   temperature). VIC-urban can facilitate multiple urban-related researches, such as identifying long-term

91   hydrothermal processes in urban systems, quantifying environmental changes resulting from urban

92   expansion, and comparing environmental variations among different urban configurations. In this article,

93   we first provide a technical description of the model coupling, process and evaluate the model in Beijing

94   regarding the land surface temperature (LST), turbulent heat fluxes, and runoff. Further, we examine the

95   sensitivity of the urban model input parameters to the urban environment (i.e., roof evaporation and

96   temperature, canyon evaporation and temperature).

2. Methodology

2.1 Urban module coupled with VIC

99   The VIC model divides a study area into Latitude-Longitude grids, with each grid representing

100   multiple land cover types and soil layers. It estimates hydrological and thermal processes for each

101   subgrid land cover type in the solution of water and energy balance (Liang et al., 1994; Liang et al.,

102   1996). However, the existing parameterization scheme ignores the unique characteristics of urban areas, such

103   as building blockage and human influence (e.g., indoor temperature, anthropogenic heat and water inputs).

104   Fortunately, VIC assigns a unique ID number to each grid, and labels each vegetation type within the target

105   grid. This enables VIC to identify and compute the subgrid land cover with individual parameters, offering

106 advantages for establishing the urban module channel.

107   We integrate an urban module into the VIC model (VIC-urban). It executes the urban module for

108 urban tiles, and follows the same calculation routine as the original VIC model for the other land cover

109 tiles. Specifically, the model uses two parameters (i.e., Gridcell and Urban_index) to identify urban tiles,

110 as shown in Figure 1. Gridcell is the ID number of the target grid. Urban_index serves as an index to

111 ascertain the presence of an urban tile, and to identify the urban tile label in the target grid. Urban_index

112 is equal to n-1 if the urban tile is the n_{th} land cover type of the target grid, and equal to -1 if there is no

113 urban tile in the grid. The VIC-urban model can thus identify the target grid and urban tile, and obtain

114 the parameters of the urban tile (i.e., the parameters of the [Urban_index+1]$_{th}$ land cover type in the

115 target grid).

116
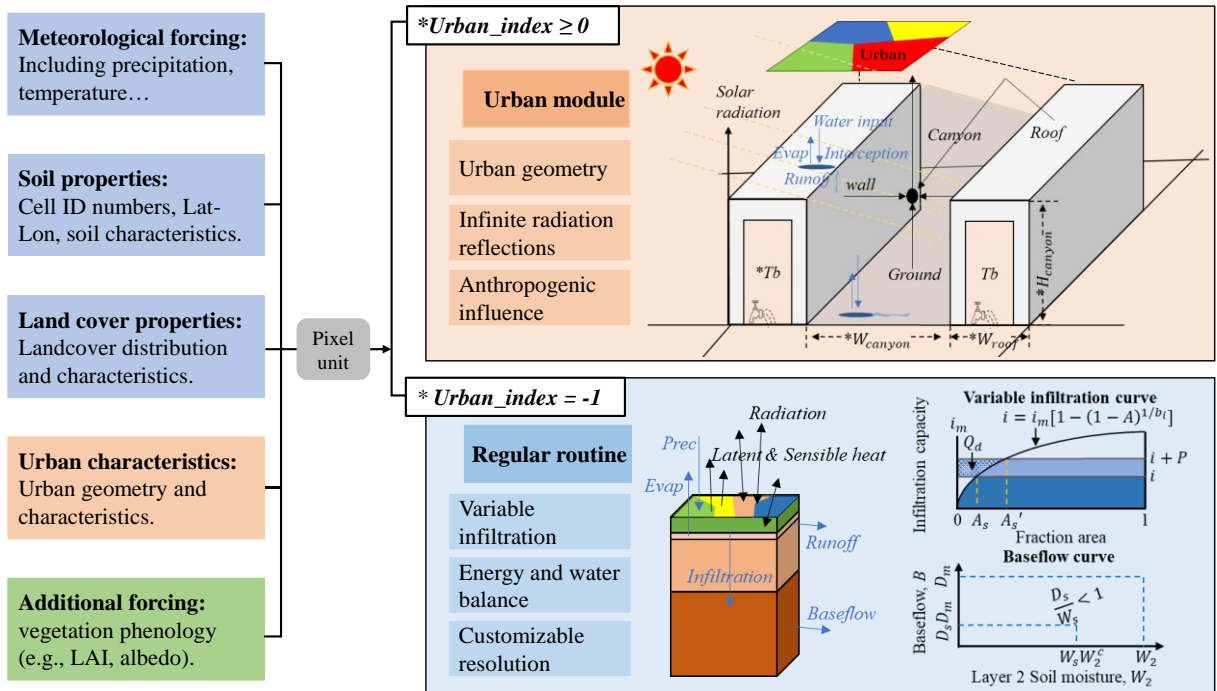
Figure 1. Diagram of the urban module coupled with the VIC model. *Wcanyon, *Wroof, *Hcanyon are
parameters that describe the urban geometry (canyon width, roof width, and canyon height). *Tb is the indoor
temperature. The parameters including *As* and *Ds* are defined by the original VIC model, and detailed
information can be found on the VIC website.

121   The urban module implemented in our study is based on the methods described in Meili et al.

122 (2020). The urban tile is parameterized by three urban geometry parameters (canyon height, canyon

123   width, and roof width) and four urban surfaces (roof, impervious ground, sunlit and shaded walls). The

124   hydrothermal fluxes and states (e.g., turbulent heat fluxes and land surface temperature) are individually

125   calculated for each urban surface, considering the urban geometry, radiative interaction, and water and

126   energy budgets. In addition, the urban module accounts for human impacts, including indoor

127   temperature, and artificial heating and irrigation. We present core formulations of the urban processes

128   and related parameters in Subsections 2.2-2.5. A more detailed explanation is included in the

129   Supplementary Document and Meili et al. (2020).

130   **2.2 Energy balance in the urban module**

131   The newly developed urban module in VIC-urban treats the energy balance differently between

132   the upper (i.e., roof) and lower canyon surfaces (i.e., ground and walls). For the roof surface, both short-

133   and longwave radiation values are calculated similar to those on bare soil, as the model assumes no

134   obstruction or radiative interaction on roofs (Supplementary Section 1.1). For the ground and walls, the

135   model first computes the incoming direct shortwave radiation as a function of the urban geometry, solar

136   position, and grid location (Supplementary Section 1.2). Then, it estimates the temperature, net absorbed

137   radiation, and turbulent fluxes of each surface according to the sky-view factor (Supplementary Section

138   1.5) and infinite radiation reflections among the various surfaces (i.e., ground, sunlit and shaded walls,

139   and sky) based on energy and water budgets. The detailed calculation method for the radiation can be

140   found in Supplementary Section 1, and that for the turbulent fluxes can be found in Supplementary

141   Section 2.

142   The energy balance of the roof, ground and wall can be calculated as:

143        $$EB_i = S_{abs,i} + L_{abs,i} - G_i - H_i - LE_i,$$ (1)

144   where EB_i is the energy balance of surface i, and $S_{abs,i}$ and $L_{abs,i}$ [W m^{-2}] are the net absorbed short-

145 and longwave radiation values, respectively, of surface i (roof, ground, and wall). G_i, H_i, and LE_i are

146 the conductive heat, sensible heat and latent heat fluxes, respectively, of surface i, and they can be

147 calculated as:

148 $$H_i = \rho_a C_p \frac{T_i - T_a}{r},$$ (2)

149 $$LE_i = \lambda \rho_a \frac{q_{sat,T_i} - q_a}{r},$$ (3)

150 $$G = -\lambda g \frac{(T_{int} - T_i)}{z},$$ (4)

151 where ρ_a [kg m^{-3}] is the air density, C_p [J kg^{-1} K^{-1}] is the specific heat capacity of air at a constant pressure,

152 T_i [K] is the temperature of surface i, [s m^{-1}] is the sum of the resistance values, λ [J kg^{-1}] is the latent heat

153 of vaporization, and q_{sat,T_i} [-] is the saturation specific humidity at temperature T_i. Notably, for the surface

154 above the canyon (i.e., canyon roof), T_a [K] and q_a [-] are the air temperature and specific humidity,

155 respectively, and for the ground and walls, T_a [K] and q_a [-] are the canyon temperature and specific

156 humidity at the canyon reference height, respectively (Supplementary Section 2.5). Moreover, λg [J K^{-1}

157 m^{-1} s^{-1}] is the heat conductivity, and z is the thickness of the layer. T_{int} is the interior building temperature,

158 which can be calculated from the outdoor and indoor temperatures based on the thermal conductivity

159 parameters (Supplementary Section 2.2).

160   The energy balance of an urban canyon can be expressed as:

161 $$EB_{can} = Q_{can} + H_g + h_{can}(H_{wsun} + H_{wshd}) + LE_g - H_{can} - LE_{can},$$ (5)

162 where EB_{can} is the energy balance of the canyon, Q_{can} is anthropogenic heat, which can be prescribed

163 according to associated observations or estimated from other formulations. H and LE are the sensible

164 heat and latent heat fluxes, respectively, and the subscripts g, can, $wsun$, and $wshd$ denote the ground,

165 canyon, sunlit wall, and shaded wall, respectively. h_{can} [-] is the canyon height normalized by the canyon

166 width (H_{can} / W_{can}).

167   The turbulent heat fluxes of canyon can be calculated as the area-weighted average of the walls and

168   ground and directly include the anthropogenic heat input (Equation 6), and the total turbulent fluxes of

169   an urban tile can be calculated as the area-weighted average of the roof and urban canyon (Equation 7):

170 $$X_{can} = w_{can} X_g + h_{can} (X_{wsun} + X_{wshd}) + Q_{can},$$ (6)

171 $$X_{urban} = f_{roof} X_{roof} + f_{can} X_{can},$$ (7)

172   where X [W m^{-2}] denotes the turbulent heat fluxes (i.e., latent or sensible heat fluxes), f_{roof} and f_{can}

173   [-] are the roof and canyon fractions, respectively, and Q_{can} [W m^{-2}] is the anthropogenic heat input.

174   The subscripts *g, can, wsun*, and *wshd* denote the ground, canyon, sunlit wall, and shaded wall,

175   respectively.

176 **2.3 Water balance in the urban module**

177   The urban module computes the water mass balance for the roof and ground individually. For the

178   roof, the incoming water is initially consumed by evaporation. Subsequently, runoff occurs when the

179   remaining water exceeds the maximum water interception capacity. Runoff can be further divided into

180   outflow runoff and runon according to a certain ratio defined by experience. Outflow runoff flows off

181   the roof and turns into incoming water for the ground, while runon remains on the roof as the incoming

182   water for the roof at the next time step. Therefore, the incoming water is equal to the precipitation and

183   runon of the previous time step.

184 $$Int_t - Int_{t-1} = P_t + Runon_{t-1} - E_t - Runoff_t - Runon_t,$$ (8)

185   where Int [mm h^{-1}] is the interception water, P [mm h^{-1}] is the precipitation, and E [mm h^{-1}] is the

186   evaporation.

187   For the ground, the incoming water flux includes precipitation, roof runoff, anthropogenic water

188   input, and runoff of the previous time step. The incoming water is first consumed by evaporation and

189   leakage and then by runoff and runon. Outflow runoff leaves the current cell, while runon remains in

190   the cell as incoming water of the next time step. Notably, the model does not consider subsurface

191 hydrological fluxes within urban tiles, such as soil moisture and baseflow, since impermeable surfaces

192 impede vertical hydrological interactions. Therefore, the grid-scale subsurface water fluxes are assumed

193 to be equal to the areal-weighted mean value of the fluxes of the other land cover types in the grid.

194 $$Int_t - Int_{t-1} = P_t + Runon_{t-1} + Runoff_{t,roof} + Q - E_t - Leak_t - Runoff_t - Runon_t, \qquad (9)$$

195 where Q [mm h^{-1}] is the anthropogenic water input, and currently can be prescribed by user-defined 12

196 monthly-cycle values, but this prescription can be improved with dynamic values according to

197 observations.

2.4 Parameters for the urban module

Table 1.
Overview of datasets for urban module in VIC model

Parameter	Unit	Description
Gridcell	N/A	**Grid cell number**
Urban_index	N/A	**Index of the veg tile containing the urban**, with respect to the list of veg tiles given in the veg param file for the current grid cell. Ranges 0~(Nveg-1) for a grid cell that contain urban, and set to -1 to denote the gird cell exclude urban.
Theta_canyon	°	**Canyon orientation**
Zatm	m	**Atmospheric forcing/reference height**
Qf_canyon	W/m^2	**Human interference:** Anthropogenic heat input
Waterf_canyon	mm/h	**Human interference:** Anthropogenic water input
Height_canyon	m	**Urban geometry:** Height of urban canyon
Width_canyon	m	**Urban geometry:** Ground width of urban canyon
Width_roof	m	**Urban geometry:** Roof width of urban canyon
Perrunoff_R/G	N/A	**Water budget:** Percentage of excess water that leaves the roof/ground as runoff
In_max_R/G	mm	**Water budget:** Maximum interception capacity of roof/ground
Kimp_R/G	mm/h	**Water budget:** Hydraulic conductivity of roof/ground
Albedo_R/G/W	N/A	**Energy budget:** Albedo roof/ground/walls
Emissivity_R/G/W	N/A	**Energy budget:** Emissivity roof/ground/walls
Lan_dry_R/G/W	W/(m*K)	**Energy budget:** Thermal conductivity of roof/ground/walls
Cv_s_R/G/W	J/(m^3*K)	**Energy budget:** Volumetric heat capacity of roof/ground/walls
Dz1_R/W	m	**Energy budget:** Thickness of first roof/wall layer
Dz2_R/W	m	**Energy budget:** Thickness of second roof/wall layer

201 For the urban module, the input data include land cover maps and urban-related parameters. The

202 land cover maps represent the locations of urban areas. The urban-related parameters are summarized

203 in Table 1. Specifically, the Gridcell and Urban_index parameters are used to identify urban tiles,

204 Qf_canyon and Waterf_canyon denote anthropogenic forcings, and the Theta_canyon, Zatm,

205   Height_canyon, Width_canyon, and Width_roof parameters define the urban geometry. Parameters such

206   as the hydraulic conductivity and maximum interception capacity albedo (i.e., Perrunoff, In_max, and

207   Kimp) are used for water budget calculation, while the other parameters (e.g., albedo, emissivity,

208   Lan_dry, Cv_s, and Dz) are used for energy budget calculation.

209   **2.5 Input data for VIC-urban**

210   In addition to the urban-related parameters listed in Table 1, the other needed input data of the VIC-

211   urban model are similar to those of the original VIC model, referring to Liang et al. (1994), Liang et al.

212   (1996), and Liang and Xie (2001). In general, the input data include topographical, meteorological

213   forcing, soil and land cover (i.e., vegetation) properties. The topographical dataset is used to delineate

214   river networks and interpolate meteorological data. Meteorological forcings provide information on

215   precipitation, maximum and minimum air temperatures, wind speed, and humidity. Soil data define the

216   initial soil moisture conditions, including variable infiltration curve and saturated hydrologic

217   conductivity, and land cover data provide vegetation conditions such as the root zone thickness and the

218   root fraction of each vegetation type.

219   In addition to the needed forcing files, the VIC model can incorporate vegetation and radiation time

220   series data (e.g., LAI, albedo, and shortwave/longwave radiation), which are particularly useful because

221   they provide dynamic information on vegetation and radiation variables. By incorporating these data,

222   the VIC model can better capture realistic land surface dynamics and energy budgets.

223   # 3. Case description

224   **3.1. Study area and data input**

225   The performance of the VIC-urban model was evaluated in simulating sensible and latent heat

226   fluxes, runoff, and land surface temperature (LST) observations in Beijing from 2005 to 2020. Beijing

227   is the capital of China, located between 39.43-41.05°N and 115.42-117.50°E. The city has experienced

228   rapid urbanization since 1980, with extensive urban coverage since 2000 (Wang et al., 2020). Beijing

229   can be divided into four functional zones with varying degrees of urbanization: the Core Functional

230   Zone (Core-Zone, with an urban fraction of ~90%), the Urban Functional Extended Zone (Extended-

231   Zone, ~70%), the New Urban Development Zone (NewDev-Zone, ~30%), and the Ecological

232   Conservation Zone (Eco-Zone, ~5%) (Figure 2). This evaluation primarily focused on the three highly

233   urbanized zones (Core-Zone, Extended-Zone, and NewDev-Zone) to demonstrate the performance of

234   VIC-urban.

235   The parameters used in the urban module were based on those reported by Jackson et al. (2010),

236   with manual calibration of the height-to-width ratio and the wall layer thickness based on MODIS LST

237   and runoff observation data. The height-to-width ratio is a highly sensitive parameter in LST modelling

238   and ranges from 0.5 to 1.1 according to the MODIS LST product. The prescribed wall layer thickness

239   ranged from 0.2 to 0.6. The values of these parameters are generally consistent with previous research

240   (Mcnorton et al., 2021; Li et al., 2016b), where the height-to-width ratio ranges from 0.75 to 1.5 and the

241   wall layer thickness ranges from 0.3 to 0.5. Supplementary Figure 2 illustrates the spatial distribution

242   maps of the urban parameters.

243   Regarding the model input data of Beijing, topographical data (i.e., the digital elevation model)

244   were obtained from the USGS with a 90-m resolution. Meteorological forcing data were produced by

245   interpolating the data obtained from observation stations of the China Meteorological Administration

246   (CMA) (Xie et al., 2015; Zhu et al., 2021). A soil map was obtained based on a 30 arc-second-resolution

247   soil characteristics dataset. The soil parameters were derived based on a Chinese soil dataset (Shangguan

248   et al., 2013; Zhu et al., 2020) and Food and Agriculture Organization (FAO) (Nijssen et al., 2001). The

249   land cover maps included base maps and urban maps. The base maps were obtained from Liu et al.

250   (2010), which were created by merging Landsat TM digital images with a spatial resolution of 1 km and

251   12 land cover types. The urban maps were obtained from Wang et al. (2020), which were created by the

252   Classification Regression Tree (CART) method using Landsat images with a spatial resolution of 30 m.

253   The land cover parameters were obtained from Zhu et al. (2020). To better reasonably reflect the land

254   cover changes in modeling, our study updated land cover maps and related parameters (e.g., the thermal

255   conductivity, volumetric heat capacity) every five years. Moreover, four satellite datasets, namely,

256   Downward Shortwave Radiation (DSR), albedo, LAI, and Fraction of Vegetation Cover (FVC), were

257   incorporated in the modelling process (Zhang et al., 2019; Liang et al., 2021) to better identify land

258   conditions and calculate turbulent heat fluxes. The four datasets used in this study are at 0.05° spatial

259   resolution. The DSR dataset is at daily temporal resolution, while the other three datasets are at 8-day

260   temporal resolution. The four datasets were obtained from Global Land Surface Satellite (GLASS)

261   products (http://www.geodata.cn/thematicView/GLASS.html) (Liang et al., 2021). The spatial/temporal

262   resolution of the VIC modelling is defined as 0.0625°/3 hours in this study. To ensure consistency, all

263   model input data were adjusted to match the same spatial resolution through a linear interpolation.

264   **3.2 Evaluation data and method**

265   The VIC-urban model underwent calibration using streamflow data from two watersheds and

266   MODIS-based LST data. Then, it was validated against observations retrieved from gauge stations and

267   MODIS data regarding sensible and latent heat, runoff, and LST. The locations of the gauge stations are

268   shown in Figure 2, and detailed information is listed in Table 2. Four measures, namely, the Nash–

269   Sutcliffe efficiency (*NSE*), Root Mean Squared Error (*RMSE*), relative bias (*Er*), and correlation

270   coefficient (*R*) were used to evaluate the performance of VIC-urban.

271   In regard to sensible and latent heat evaluation, three flux towers were used, namely, the Beijing,

272 Daxing, and Miyun stations. In particular, the Beijing station is located in the central part of Beijing and

273 is widely used to investigate urban turbulence characteristics (Liu et al., 2020b; Ji et al., 2021). To

274 calibrate and validate the simulated runoff, streamflow data from three stations were used, namely,

275 Boyachang (BYCH), Qianxinzhuang (QXZH), and Wenyu (WY). Their corresponding watersheds are

276 located in the northern part of Beijing and contain various land cover types, including urban, forest, crop,

277 and grass (Figure 2). The observed discharge data of the QXZH and BYCH stations were separated into

278 two periods for model calibration and validation, whereas the observed discharge of the WY station was

279 compared to the simulated runoff for the entire period due to the availability of only yearly data.

280 **Table 2.**

281 Validation data used in this work

Name	Source	Detailed information
Sensible heat	NCDDC, IAP	Beijing, 2011-2013, daily
Latent heat	NCDDC, IAP	Miyun, 2018-2010, daily
		Daxing, 2018-2010, daily
Runoff	AHRPR	QXZH, 2006-2009, monthly
		BYCH, 2006-2014, monthly
		WY, 2005-2017, yearly
LST	CMA, MODIS	14 ground stations, daily
		MOD11A2, eight-days

NCDDC, National Cryosphere Desert Data Center; IAP, Institute of Atmospheric Physics; AHRPRC, Annual Hydrological Report for the P.R. China, CMA, China Meteorological Administration; MODIS, MODerate-resolution Imaging Spectroradiometer; QXZH, Qianxinzhuang; BYCH, Boyachang; WY, Wenyu.
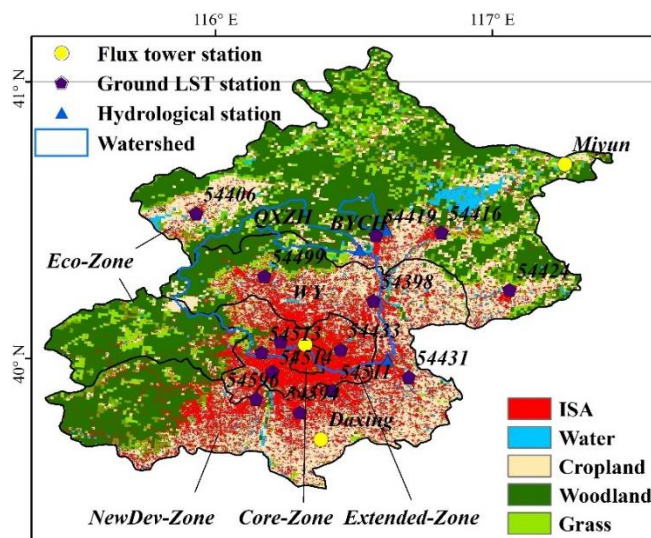
282

283 **Figure 2.** Location of Beijing and the flux tower stations, hydrological stations and watersheds, and ground
284 LST stations, with the 2015 land cover map as the background.

285   Regarding LST evaluation, we obtained data from fourteen ground-based stations and one satellite-

286   based product. At the ground-based stations of the CMA, platinum resistance sensors are used that are

287   semi-buried in soil to measure the daily temperature at the skin surface. Among the stations, three

288   stations provide long-term coverage data for the 2005 to 2020 period, while the remaining stations

289   provide data covering the 2016 and 2020 period. The satellite-based LST product of the Terra Moderate

290   Resolution   Imaging   Spectroradiometer   (MODIS)   was   adopted,   i.e.,   MOD11A2   v006

291   (https://modis.gsfc.nasa.gov/). MODIS LST data constitute one of the most widely used data for LST

292   studies (Bounoua et al., 2015; Zhou et al., 2010; Liu et al., 2020a; Morabito et al., 2021; Zhou et al.,

293   2018). The MODIS has provided two instantaneous LST estimates (10:30 and 22:30 local solar time)

294   every eight days since 2000, with a spatial resolution of 1 km. In our work, the simulated LST was

295   averaged every eight days for comparison with the MODIS data. The simulated LSTs from 9:00-12:00

296   and 21:00-24:00 were compared with the MODIS data for 10:30 and 22:30, assumed to represent the

297   morning and evening times, respectively. Notably, the gauge-based measurements were obtained at the

298   point scale, which is smaller than the model output resolution. To resolve the mismatch in the spatial

299   scale, the evaluation was conducted at the subgrid scale with the same land cover type in the

300   corresponding grid.

301   **3.3 Sensitivity analysis**

302   To examine the sensitivity of the model parameters to changes in the urban environment. Four

303   fluxes, namely, roof temperature, roof evaporation, canyon temperature, and canyon evaporation, were

304   used as indicators of the urban environment. A single grid cell with high urban coverage was selected,

305   and its input values were used as default values. The urban input parameters range from 70% to 130%

306   of the default values in 6% change steps. The specific parameters and their values are listed in

307   Supplementary Table 1.

308   The sensitivity analysis covered 6 years (2015-2020) and was conducted at the annual scale, as

309   well as for the winter (December to February of the next year) and summer (June to August) seasons.

310   The sensitivity coefficient Sc can be calculated as (Beven, 1979):

311    $$Sc = \lim_{X \to 0} \frac{\Delta Y / Y}{\Delta X / X} \times 100\%,$$ (10)

312   where X is the input parameter that affects the urban environment (Y). A positive (or negative) Sc value

313   suggest that Y is enhanced (or reduced) with increasing X.

4. Results

4.1 Land surface temperature

316   The simulated LST was calibrated against the MODIS LST and evaluated using two ground

317   observations and the MODIS LST dataset. As shown in Figure 3, the simulated LST exhibited similar

318   spatial patterns to those of the MODIS estimates for both the morning and evening times at the city

319   center. At the morning time, both the VIC-urban model and MODIS data exhibited high LST values in

320   Core-Zone and the southern part of Extended-Zone. At the evening time, the VIC-urban model

321   simulations failed to capture the scattered LST patterns in Eco-Zone and the southwestern part of

322   NewDev-Zone. This disagreement may be attributed to the relatively low urban fraction in these areas,

323   given that our work mainly focused on the calculation of urban-related processes. Other than in these

324   areas, the model could accurately produce a similar LST distribution relative to the MODIS LST data

325   in Core-Zone and Extended-Zone.

326   In terms of temporal comparison, the simulated LST exhibited a high performance in all of Beijing

327   and the three subzones (Core-Zone, Extended-Zone, and NewDev-Zone). As shown in Figures 4 and 5,

328   the simulated LST indicated similar yearly dynamics and mean monthly cycles relative to the MODIS

329 LST data. The *R* values were over 0.8, and the *RMSE* and *Er* values were lower than 0.5℃ and 2.3%

330 for the morning and evening times, respectively. These results indicated that the simulated LST values

331 closely captured the temporal variations and spatial patterns of the MODIS LST data.
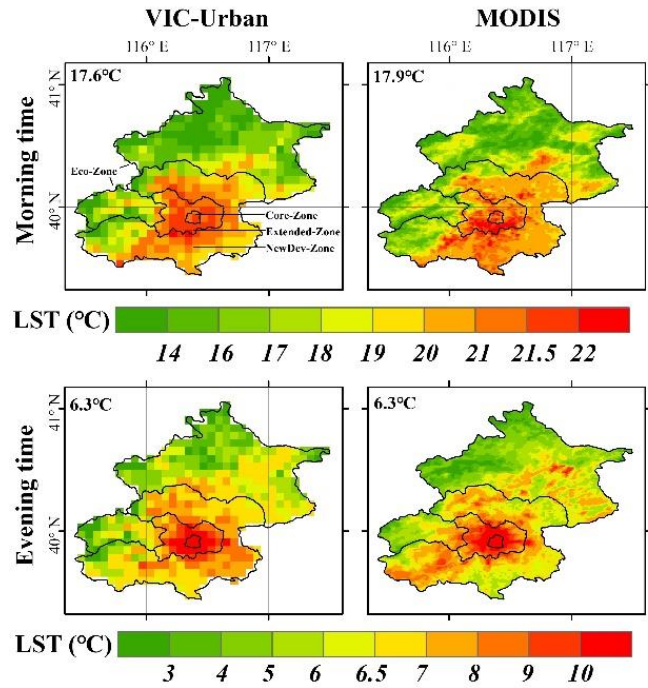
332
333 **Figure 3.** Spatial distribution of the simulated LST compared to the MOD11A2 product, with the average
334 LST shown in the upper left of the figure.

335
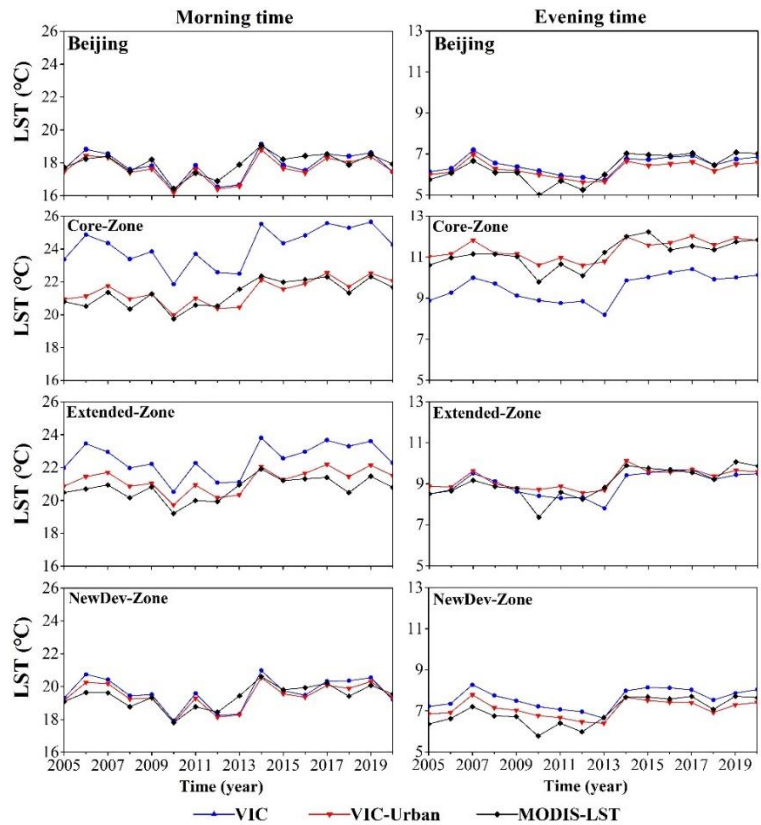
Figure 4. Yearly dynamics of the simulated LST compared to the MOD11A2 product for Beijing and the three functional zones (i.e., Core-Zone, Extended-Zone, and NewDev-Zone).
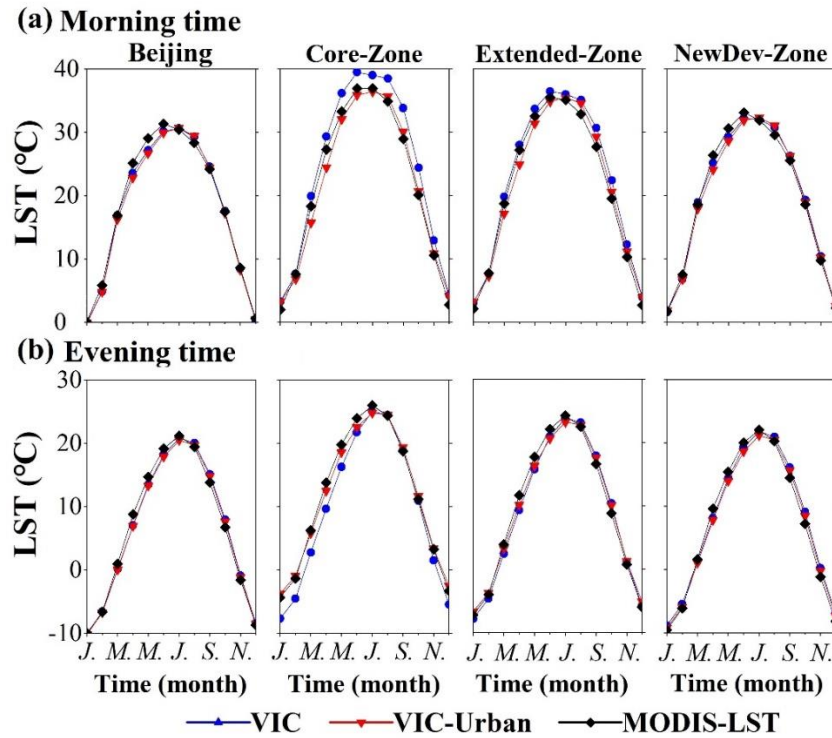
Figure 5. Mean monthly cycle of the simulated LST compared to the MOD11A2 product for Beijing and the three functional zones (Core-Zone, Extended-Zone, and NewDev-Zone).

In regard to station-scale comparison, the model produced satisfactory LST estimates for the annual dynamics and during the winter and summer seasons (Figure 6). Specifically, the overall *RMSE* was lower than 1.9 °C, *R* was higher than 0.9, and *Er* was lower than 7% at the annual scale. During the winter and summer seasons, the *RMSE* values were lower than 1.7 °C, the *R* values were higher than 0.7, and *Er* was approximately 24.9% in winter and −0.2% in summer. The high *Er* value during the winter season could be attributed to the low average winter LST. The comparison at each site also indicated promising results (Table 3), with all *Er*s values lower than 12% and all *RMSE* values below 1.8 °C. It is important to note that the stations generally provided only five available values, i.e., annual data for the 2016 to 2020 period. Nevertheless, the *R* values for all the stations consistently exceeded 0.4, indicating the satisfactory performance of the VIC-urban model.
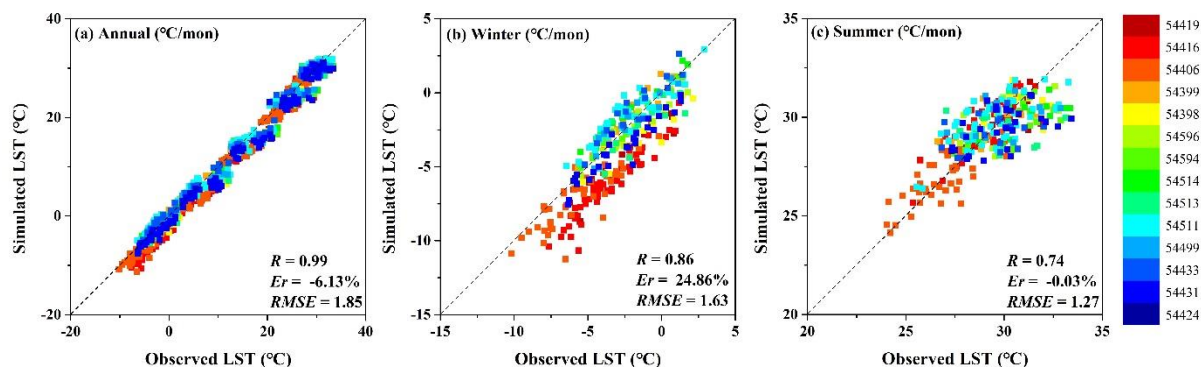
Figure 6. Monthly simulated LST validated against 14 ground-based observation stations, which are marked in different colours.

Table 3.
The simulated LSTs from VIC-urban and VIC models are validated by 14 ground-based observations at an annual scale. The results of three indexes (*Er*, *R* and *RMSE*) are shown in the table, with the better results underlined.

Station	*Er* (%)		*R*		*RMSE*	
	VIC–urban	VIC	VIC–urban	VIC	VIC–urban	VIC
54419	−7.78	-9.56	0.64	0.15	1.19	1.47
54416	−11.28	-10.58	0.79	0.89	1.63	1.52
54406	−8.37	-12.75	0.87	0.65	1.06	1.64
54399	0.29	8.61	0.92	0.69	0.12	1.28
54398	−8.24	-13.54	0.61	0.56	1.34	2.17
54596	−6.54	-5.29	0.63	0.68	1.07	0.88
54594	−7.10	-3.77	0.48	0.92	1.13	0.60
54514	−5.21	1.18	0.92	0.73	0.84	0.28
54513	−5.46	-3.54	0.80	0.51	0.85	0.67
54511	−1.38	-3.97	0.73	0.34	0.61	2.00
54499	−1.88	-1.71	0.88	0.72	0.37	0.40
54433	−0.87	3.09	0.40	0.38	0.35	0.58
54431	−5.24	-7.59	0.85	0.01	0.85	1.24
54424	−11.74	-12.44	0.77	0.46	1.76	1.88

4.2 Runoff

The model was further calibrated using the streamflow data for the QXZH and BYCH watersheds and validated against the streamflow data for the WY, QXZH, and BYCH watersheds (Figure 7). During the calibration period, the *NSE* and *R* values for the QXZH and BYCH watersheds were approximately 0.5 and 0.8, respectively, and the *Er* and *RMSE* values were below 10% and 4 mm/month, respectively, for both watersheds. During the validation period, the simulated runoff showed a high correlation with the observed data of the three watersheds, with *R* ranging from 0.8 to 0.9 and *NSE* ranging from 0.6 to 0.8. The *RMSE* reached approximately 4 mm/month at QXZH, 5 mm/month at BYCH, and 42 mm/yr

366   at WY. The *Er* values were approximately 12% (QXZH), 29% (BYCH), and −9.5% (WY), respectively.

367   The overestimations at QXZH and BYCH and the underestimation at WY could likely be attributed

368   to the limitations of the VIC-urban model in considering human activities. Specifically, the model did

369   not consider water allocation for industrial use in the upstream region of the city (QXZH and BYCH)

370   or the impact of industrial and domestic wastewater at the city centre (WY). *Er* of the WY watershed

371   showed an increasing trend, particularly after 2013, which could be attributed to the increasing

372   wastewater discharge. Despite these limitations, the VIC-urban model demonstrated an acceptable

373   performance in simulating runoff.
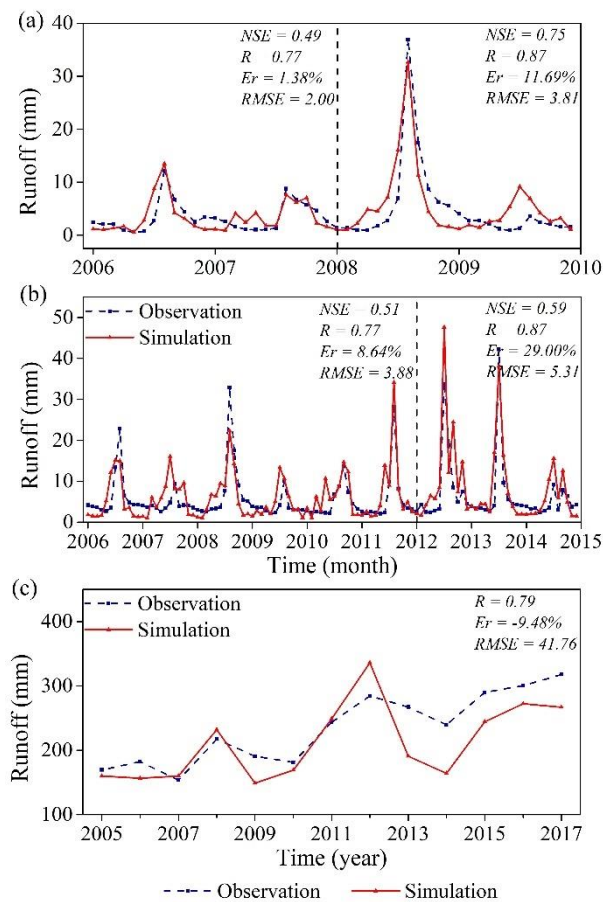
374
375 **Figure 7.** Evaluation of the simulated runoff. (a) QXZH; (b) BYCH; and (c) WY. The dark dotted line divides
376 the data into the calibration period (before) and validation period (after).

377 **4.3 Turbulent heat fluxes**

378   The VIC-urban model was evaluated regarding the sensible and latent heat using the observed

379   data of three stations: Beijing, Miyun, and Daxing. As shown in Figure 8a, the simulated sensible heat

380   flux agrees well with the observed value at the Beijing station. R is approximately 0.65, and the $RMSE$

381   and Er are below 22 W/m^2 and 25%, respectively. Regarding the latent heat (Figure 8c, d), the

382   simulated values exhibit high correlations (Rs) with the observed data at the Miyun stations ($\sim$ 0.86),

383   and R at the Daxing station is approximately 0.65. Additionally, the $RMSE$ values are below 30 W/m^2

384   for all stations, and the Er values vary between −21% and −17%.
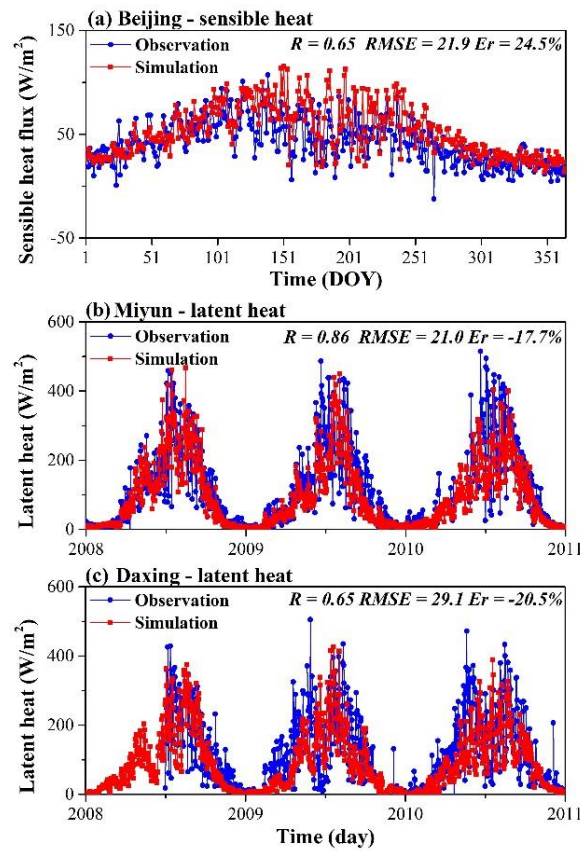
385
386 **Figure 8.** Evaluation of the sensible and latent heat flux simulations. (a) sensible heat flux at the Beijing flux
387 tower; (b) latent heat flux at the Miyun flux tower; (c) latent heat flux at the Daxing flux tower.

388 **4.4 Comparison with the original VIC**

389   The performance of the VIC-urban model and the original VIC model were compared in terms of

390 the simulated turbulent heat fluxes, LST, and runoff. As shown in Figure 9, the simulation results of the

391 VIC-urban and the VIC models showed similar patterns at the Miyun and Daxing stations, as the two

392 stations are located in suburban areas. The VIC-urban model mainly focuses on improving the model

393 performance in urban areas rather than suburban areas. For the Beijing station, which is located at the

394 site with a high degree of urbanization, VIC-urban provided a better performance. Specifically, the VIC-

395 urban model yielded a smaller *RMSE* (~12.7 W/m^2) for the sensible heat flux than that of the VIC model

396 (~15.7 W/m^2), and attained a higher correlation (~0.93) than the VIC model (~0.81).

397   In terms of the LST, the VIC-urban model simulations show a lower discrepancy from the MODIS

398 product, especially at the city centre, and the average LST difference is less than 0.5 ℃ for both the

399 morning and evening times (Figure 10). However, the average LST difference is larger than 1.8 ℃ when

400 using the VIC model. Regarding temporal comparison (Figures 3 and 4), the VIC-urban model

401 simulations show similar patterns to those in the MODIS data, while the VIC model simulations tend to

402 overestimate the LST at the morning time and underestimate the LST at the evening time in Extended-

403 Zone. The VIC-urban model also outperforms the VIC model at the station scale, as indicated by the

404 higher *R* and lower *Er* and *RMSE* values (Table 3).
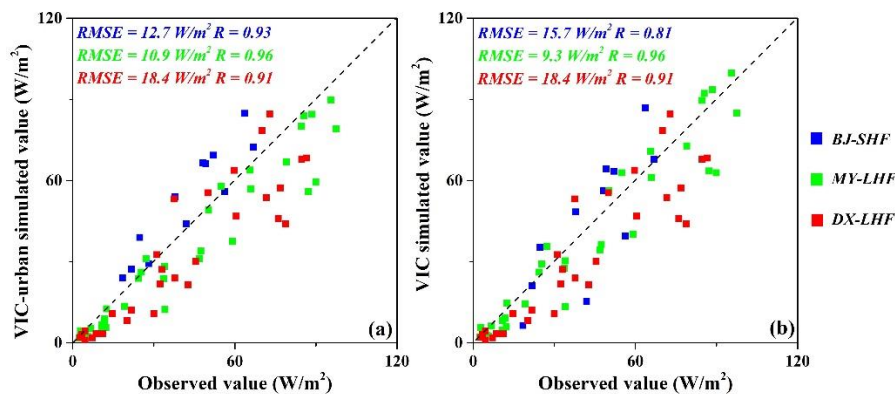
406 **Figure 9.** Simulated yearly turbulence heat fluxes of the VIC-urban and VIC models compared to the
407 observed data. The blue points denote the comparison of the sensible heat flux at the Beijing station, and the
408 green and red points denote the comparisons of the latent heat flux at the Miyun and Daxing stations,
409 respectively.

410   Regarding runoff (Figure 11), the VIC-urban and VIC models exhibit similar performance levels

411 for both the BYCH and QXZH watersheds. However, the VIC model obviously underestimates runoff

412 in the WY watershed, which has a high urban coverage. The *RMSE* values of the VIC and VIC-urban

413 model simulations for WY are 98.3 and 41.8 mm/yr, respectively. Based on the comparisons above, it is

414 evident that the VIC-urban model outperforms the original VIC model in analyzing urban-related

415 processes and can capture more realistic hydrological and thermal processes in cities.
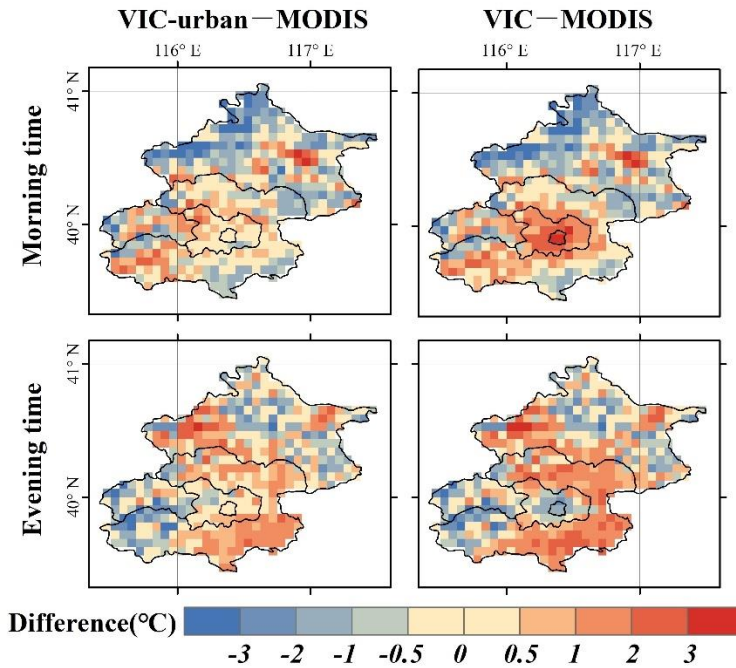
416

417 **Figure 10.** Spatial distribution of the LST differences between the MODIS LST and the simulated LST of
418 the VIC-urban model (left), and between MODIS LST and the simulated LST of the VIC model.
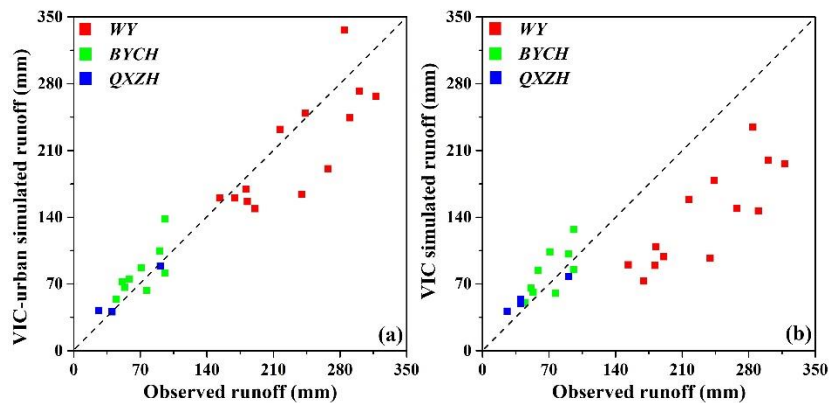
419

420 **Figure 11.** Simulated yearly runoff of the VIC-urban and VIC models compared to the observed data. The
421 red, green, and blue points denote the comparisons in the WY, BYCH, and QXZH watersheds, respectively.

422 **4.5 Sensitivity analysis**

423   We further calculated the sensitivity of the hydrothermal process-related urban input parameters,

424   that is, we calculated the impact on four indicators (i.e., roof temperature and evaporation and canyon

425   temperature and evaporation). Regarding the roof (Figure 12 a, b), Emissivity_R and Albedo_R

426   generally exhibited high sensitivity to the roof temperature, with sensitivity coefficients of −21% and

427   −11%, respectively. The changes in In_max_R, Perrunoff_R, Emissivity_R and Albedo_R exerted

428   obvious impacts on roof evaporation, with values of 41%, −19%, −10%, and −8%, respectively.

429   Regarding the sensitivity of the canyon environment (Figure 12 c, d), Width_canyon (−5%) and

430   Width_roof (4%) imposed the greatest impact on the canyon temperature, followed by Emissivity_W

431   (−4%), Dz_W (−3%), Lan_dry_W (3%), and Albedo_W (−2%). In terms of canyon evaporation,

432   Width_canyon (44%) and In_max_G (37%) yielded the highest impact, followed by Perrunoff_G

433   (−29%), Kimp_G (−23%), Albedo_G (−20%), Emissivity_W (16%) and Albedo_W (14%). An

434   interesting finding is that the wall parameters (e.g., Emissivity_W, Albedo_W) generally imposed a

435   greater influence on the canyon temperature, while the ground parameters exerted a higher influence on

436   canyon evaporation. The sensitivity coefficients of all parameters are listed in Supplementary Table 2.

437   Supplementary Figures 3 and 4 show the urban environment (roof and canyon temperature and

438   evaporation) changes with increasing parameter value during the summer and winter seasons. The urban

439   environment exhibited diverse patterns under parameter increase, rather than simply following linear

440   trajectories. An interesting discovery is that the Dz_R and Lan_dry_R parameters showed opposite

441   impacts on the roof temperature during the summer and winter seasons. This inconsistency could be

442   attributed to their role in regulating heat transfer between indoor and outdoor environments. Specifically,

443   indoor temperatures are higher than outdoor temperatures in winter and lower in summer. A higher

444   thermal conductivity (i.e., higher Lan_dry_R and lower Dz_R values) will increase the outdoor surface

445   temperature in winter and decrease it in summer. Similarly, the parameters related to heat conduction

446   (e.g., Dz_W and Lan_dry_G) in canyon exerted contrasting impacts on the canyon environment during

447   the summer and winter seasons. Moreover, parameters such as albedo and emissivity directly exerted

448   negative impacts on both the roof and canyon temperatures and evaporation levels. Their effects on roofs

449   are generally similar between winter and summer, and their impact on canyons is more pronounced in

450   summer than in winter.

451
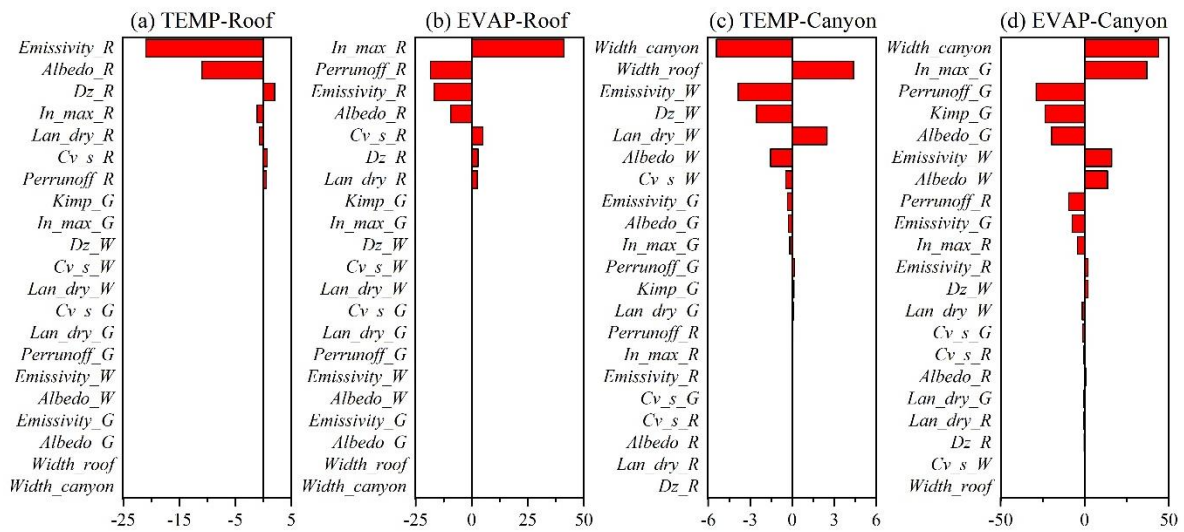
Figure 12. Sensitivity coefficients of the parameters to the urban environment: (a) Roof temperature; (b) roof evaporation; (c) canyon temperature; and (d) canyon evaporation.

5. Discussion

5.1. Enhanced performance of VIC-urban in urban systems

456   The urban module described above is among the first attempts to establish a systematic urban

457   environment in the solution of the energy and water budget in the VIC model. The VIC-urban model

458   incorporates detailed representations of urban canyons, urban geometry, and human influences. The

459   model therefore provides favourable estimates of various components of the energy and water balance

460   (e.g., surface runoff, evaporation, and LST) of each urban surface (i.e., roof, canyon, ground, and sunlit

461   and shaded walls).

462   In each urban tile, the VIC-urban model calculates the incoming radiation of each surface based on

463 geographic information, solar time, and geometric parameters. It then estimates energy budgets using

464 an iterative approach that considers radiative interactions and energy balance principles(Meili et al.,

465 2020). In water balance calculation, the model simulates the hydrological processes of the ground and

466 roof individually and assumes that roof runoff contributes to the groundwater input. Additionally, given

467 the distinct characteristics of urban areas, where excess water on a given surface tends to remain in place

468 rather than immediately exiting the system (e.g., flat roofs and ground), the model includes a runon

469 component to more comprehensively represent water movement in urban environments.

470   The VIC-urban model was assessed based on the data of multiple gauge stations and MODIS LST

471 data and compared to the original VIC model in Beijing urban areas. The results indicated that the VIC-

472 urban model achieves excellent performance, with *RMSE* values below 0.5 and 1.8 ℃ relative to the

473 MODIS LST and gauge station data, respectively, and lower than 30 W/m^2 and 6 mm/month in turbulent

474 heat and runoff evaluation, respectively. Importantly, the VIC-urban model outperforms the original VIC

475 model in urban areas. It largely reduces the discrepancy between the simulated and observed values,

476 successfully capturing higher LST and runoff values at the urban center. These findings suggest that the

477 VIC-urban model is a valuable tool for reliable analysis of urban areas.

478 **5.2 Advantages of the VIC-urban model**

479   The development of the VIC-urban model provides a new urban modelling option. It employs the

480 canyon concept, which has been widely used in UCMs and coupled models (Oleson and Feddema, 2020;

481 Li et al., 2016b; Sun and Grimmond, 2019). Most UCMs, such as the Surface Urban Energy and Water

482 Balance Scheme (SUEWS) (Järvi et al., 2011), are primarily focus on water and energy balances on

483 urban impervious surface, and generally applied at small spatial scale, such as a single city. Moreover,

484 UCMs often neglect heterogeneity within urban areas (Kusaka et al., 2001; Meili et al., 2020). In contrast,

485   the VIC-urban model is able to simulate hydrothermal processes for multiple land cover types, and has

486   the strength for large-scale applications beyond urban areas (e.g., regional and global scales). VIC-urban

487   offers high customizability with urban configurations and simulates hydrothermal processes at the grid

488   cell scale. It can merge hydrothermal inputs at the subcity scale to enhance its potential for predicting

489   water and energy balances in complex urban systems.

490   Large-scale urban models provide advantages in detecting hydrothermal dynamics in urban

491   environments due to their consideration of surface heterogeneity within a city. For instance, the CLMU

492   model incorporates a building energy model that considers convection and longwave radiation exchange

493   with interior building surfaces (Oleson and Feddema, 2020). The LM3-UCM model can simulate carbon

494   exchange and considers dynamic transitions between urban, agricultural, and unmanaged tiles (Li et al.,

495   2016b). However, these models often use constant land cover and radiation parameters over time. The

496   VIC-urban model can continuously capture land cover and radiation dynamics by integrating remote

497   sensing products. Furthermore, it incorporates a comprehensive thermally conductive framework that

498   considers three distinct layers (i.e., outdoor environment, interior building, and indoor environment) and

499   two vertical wall layers. These features are crucial for identifying long-term urban-induced

500   environmental changes and providing a comprehensive understanding of the urban environment.

501   **5.3 Limitations**

502   The current version of the VIC-urban model has certain limitations. First, the model lacks the

503   water and energy balance related to snow melting, as well as certain anthropogenic disturbances (e.g.,

504   drainage systems, air conditioning, and car exhaust) (Liu et al., 2021). The model also simplifies

505   anthropogenic heat and water impacts, which are user-defined and represented by a constant setting and

506   12-month cycle values, respectively. However, these anthropogenic influences fluctuate over time, such

507   as anthropogenic heat input in office areas varying between weekdays and weekends. These factors may

508   impose a significant impact on the urban environment, and need to be further studied given the

509   availability and accuracy of data and the feasibility of methods (Yousefi Sohi et al., 2024). Second, the

510   model does not consider horizontal interactions between land cover types and water and energy transfer

511   in the subsoil beneath impervious surfaces due to impermeable characteristics. Third, the module does

512   not explicitly formulate the type of urban vegetation (i.e., vegetation or trees in cities), which may play

513   an important role in the hydrology and energy cycle of cities (Meili et al., 2020; Wang et al., 2018).

514   Nevertheless, the VIC-urban model divides the study area of interest into grids and categorises urban

515   vegetation as forests and/or grasslands, thus estimating the water and energy balance.

516   The validation of the turbulent heat flues was not sufficient to reflect the model performance due

517   to the scarcity of station data. However, the model was further validated using runoff and LST data

518   obtained from gauge stations and the MODIS product. These hydrothermal fluxes and states can be

519   cross-verified based on the principles of water and energy balance, proving the reliability of VIC-urban

520   in representing the complexity of urban environments. In addition, the VIC-urban model introduces new

521   parameters (Table 1) that should be estimated or calibrated before the simulation, and these parameters

522   may cause substantial uncertainties. Notably, parameters such as In_max_R (maximum infiltration rate)

523   and height-to-width ratio are influential on estimating urban temperature and evaporation patterns, as

524   illustrated in Subsection 4.5. Cities worldwide exhibit diverse configurations and various human

525   influences, leading to differing empirical parameters of influence. The VIC-urban model therefore

526   requires more evaluations in cities with diverse urban environments.

6. Conclusion

528   In this study, we developed a new urban module in the VIC model, demonstrated its reliability and

529 estimated the sensitivity of the model parameters. Adopting Beijing as an evaluation site, the VIC-urban

530 model showed promising performance regarding the simulation of sensible heat, latent heat, runoff, and

531 LST. Moreover, the VIC-urban model could better capture the LST and runoff patterns at the city centre

532 than the original VIC model. The sensitivity analysis revealed that the parameters of emissivity (i.e.,

533 Emissivity_R) and maximum interception capacity of the roof (i.e., In_max_R) generally exert the

534 greatest impacts on the roof temperature and evaporation, respectively, and the height-to-width ratio

535 imposed the highest impact on the canyon temperature and evaporation.

536 The current version of the VIC-urban model still holds substantial uncertainties due to its

537 parameters and related processes and the lack of consideration of human disturbances (anthropogenic

538 heat and water inputs), horizontal interactions, and snow dynamics. However, our work is among the

539 first attempts to establish a systematic urban estimation within the VIC model, and the model is suitably

540 formulated with detailed subcity configurations, human influences, and radiative balance and

541 interactions. By considering the unique characteristics of urban areas and land cover and radiation

542 dynamics, the VIC-urban model provides a more realistic representation of urban hydrology and thermal

543 dynamics. Therefore, the model can be a valuable tool for detecting and understanding water and energy

544 processes in urban areas, and for improving the prediction of hydrothermal fluxes and states of the urban

545 environment.

546 **Code and data availability**

547 The codes of VIC-urban, and example file for urban parameters are available at

548 https://doi.org/10.5281/zenodo.10258321. The original VIC model is available at

549 https://vic.readthedocs.io/en/master/Overview/ModelOverview/, and the urban module refers to

550 https://doi.org/10.5194/gmd-13-335-2020 (Meili et al., 2020). The MODerate-resolution Imaging

Spectroradiometer (MODIS) datasets used in this study are available at https://modis.gsfc.nasa.gov/. The

Global LAnd Surface Satellite (GLASS) products are available at www.glass.umd.edu.

Author contribution

Yibing Wang designed and implemented the model, performed the analysis, and wrote the manuscript.

Xianhong Xie proposed and supervised the study, wrote and revised the manuscript. Bowen Zhu, Arken

Tursun, Fuxiao Jiang created the figures and wrote Supplementary Section 1. Yao Liu, Dawei Peng, Buyun

Zheng wrote Supplementary Section 2. All authors gave comments and discussions to the study.

Competing interests

The contact author has declared that neither of the authors has any competing interests.

Acknowledgement

This study was supported by grants from the National Natural Science Foundation of China (No.

42271021) and Open Fund of State Key Laboratory of Remote Sensing Science and Beijing Engineering

Research Center for Global Land Remote Sensing Products (No. OF202204).

Reference

Best, M. J. and Grimmond, C. S. B.: Key conclusions of the first international urban land surface model comparison project, Bulletin of the American Meteorological Society, 96, 805–819, https://doi.org/10.1175/BAMS-D-14-00122.1, 2015.

Beven, K.: A sensitivity analysis of the Penman-Monteith actual evapotranspiration estimates, Journal of Hydrology, 44, 169-190, 1979.

Bierkens, M. F. P., Bell, V. A., Burek, P., Chaney, N., Condon, L. E., David, C. H., de Roo, A., Döll, P., Drost, N., Famiglietti, J. S., Flörke, M., Gochis, D. J., Houser, P., Hut, R., Keune, J., Kollet, S., Maxwell, R. M., Reager, J. T., Samaniego, L., Sudicky, E., Sutanudjaja, E. H., van de Giesen, N., Winsemius, H., and Wood, E. F.: Hyper-resolution global hydrological modelling: what is next?, Hydrological Processes, 29, 310-320, 10.1002/hyp.10391, 2015.

Bounoua, L., Zhang, P., Mostovoy, G., Thome, K., Masek, J., Imhoff, M., Shepherd, M., Quattrochi, D., Santanello, J., Silva, J., Wolfe, R., and Toure, A. M.: Impact of urbanization on US surface climate, Environmental Research Letters, 10, 084010, 10.1088/1748-9326/10/8/084010, 2015.

Chen, J., Bu, J., Su, Y., Yuan, M., Cao, K., and Gao, Y.: Urban evapotranspiration estimation based on anthropogenic activities and modified Penman-Monteith model, Journal of Hydrology, 610, 127879, 10.1016/j.jhydrol.2022.127879, 2022.

Hersbach, H., Bell, B., Berrisford, P., Hirahara, S., Horányi, A., Muñoz-Sabater, J., Nicolas, J., Peubey, C., Radu, R., Schepers, D., Simmons, A., Soci, C., Abdalla, S., Abellan, X., Balsamo, G., Bechtold, P., Biavati, G., Bidlot, J., Bonavita, M., Chiara, G., Dahlgren, P., Dee, D., Diamantakis, M., Dragani, R., Flemming, J., Forbes, R., Fuentes, M., Geer, A., Haimberger, L., Healy, S., Hogan, R. J., Hólm, E., Janisková, M., Keeley, S., Laloyaux, P., Lopez, P., Lupu, C., Radnoti, G., Rosnay, P., Rozum, I., Vamborg, F., Villaume, S., and Thépaut, J. N.: The ERA5 global reanalysis, Quarterly Journal of the Royal Meteorological Society, 146, 1999-2049, 10.1002/qj.3803, 2020.

Huang, S., Zhang, X., Yang, L., Chen, N., Nam, W.-H., and Niyogi, D.: Urbanization-induced drought modification: Example over the Yangtze River Basin, China, Urban Climate, 44, 101231, 10.1016/j.uclim.2022.101231, 2022.

Jackson, T. L., Feddema, J. J., Oleson, K. W., Bonan, G. B., and Bauer, J. T.: Parameterization of Urban Characteristics for Global Climate Modeling, Annals of the Association of American Geographers, 100, 848-865, 10.1080/00045608.2010.497328, 2010.

Järvi, L., Grimmond, C. S. B., and Christen, A.: The Surface Urban Energy and Water Balance Scheme (SUEWS): Evaluation in Los Angeles and Vancouver, Journal of Hydrology, 411, 219-237, 10.1016/j.jhydrol.2011.10.001, 2011.

Ji, P., Yuan, X., Liang, X. Z., Jiao, Y., Zhou, Y., and Liu, Z.: High-Resolution Land Surface Modeling of the Effect of Long-Term Urbanization on Hydrothermal Changes Over Beijing Metropolitan Area, Journal of Geophysical Research: Atmospheres, 126, 10.1029/2021jd034787, 2021.

Jiang, F., Xie, X., Wang, Y., Liang, S., Zhu, B., Meng, S., Zhang, X., Chen, Y., and Liu, Y.: Vegetation greening intensified transpiration but constrained soil evaporation on the Loess Plateau, Journal of Hydrology, 614, 128514, 10.1016/j.jhydrol.2022.128514, 2022.

Kusaka, H., Kondo, H., and Kikegawa, Y.: A simple single-layer urban canopy model for amtspheric models: Comparison with multi-layer and slab models, Boundary-Layer Meteorology, 2001, 101., 101, 329–358, 2001.

Li, D., Malyshev, S., and Shevliakova, E.: Exploring historical and future urban climate in the Earth System Modeling framework: 1. Model development and evaluation, Journal of Advances in Modeling Earth Systems, 8, 917-935, 10.1002/2015ms000578, 2016a.

Li, D., Malyshev, S., and Shevliakova, E.: Exploring historical and future urban climate in the Earth System Modeling framework: 2. Impact of urban land use over the Continental United States, Journal of Advances in Modeling Earth Systems, 8, 936-953, 10.1002/2015ms000579, 2016b.

Li, X., Fan, W., Wang, L., Luo, M., Yao, R., Wang, S., and Wang, L.: Effect of urban expansion on atmospheric humidity in Beijing-Tianjin-Hebei urban agglomeration, Science of the total environment, 759, 144305, 10.1016/j.scitotenv.2020.144305, 2021.

Liang, S., Cheng, C., Jia, K., Jiang, B., Liu, Q., Xiao, Z., Yao, Y., Yuan, W., Zhang, X., Zhao, X., and Zhou, J.: The Global LAnd Surface Satellite (GLASS) products suite, Bulletin of the American Meteorological Society, 102, E323-E337, 10.1175/BAMS-D-18-0341.1, 2021.

Liang, X. and Xie, Z.: A new surface runoff parameterization with subgrid-scale soil heterogeneity for land surface models., Advances in Water Resources, 24, 1173-1193, 10.1016/S0309-1708(01)00032-X, 2001.

Liang, X., Wood, E. F., and Lettenmaier, D. P.: Surface soil moisture parameterization of the VIC-2L model: evaluation and modification., Global and Planetary Change, 13, 195-206, 10.1016/0921-8181(95)00046-1, 1996.

Liang, X., Lettenmaier, D. P., Wood, E. F., and Burges, S. J.: A simple hydrologically based model of land surface water and energy fluxes for general circulation models, Journal of Geographical Research, 99, 14415-14428, 10.1029/94JD00483 1994.

Liu, B., Xie, Z., Liu, S., Zeng, Y., Li, R., Wang, L., Wang, Y., Jia, B., Qin, P., Chen, S., Xie, J., and Shi, C.: Optimal water use strategies for mitigating high urban temperatures, Hydrology and Earth System Sciences, 25,

387-400, 10.5194/hess-25-387-2021, 2021.

Liu, J., Zhang, Z., Xu, X., Kuang, W., Zhou, W., Zhang, S., Li, R., Yan, C., Yu, D., and Wu, S.: Spatial patterns and driving forces of land use change in China during the early 21st century, Journal of Geographical Sciences, 20, 483-494, 10.1007/s11442-010-0483-4, 2010.

Liu, Q., Zhang, S., Zhang, H., Bai, Y., and Zhang, J.: Monitoring drought using composite drought indices based on remote sensing, Science of the total environment, 711, 134585, 10.1016/j.scitotenv.2019.134585, 2020a.

Liu, X., Zhou, Y., Yue, W., Li, X., Liu, Y., and Lu, D.: Spatiotemporal patterns of summer urban heat island in Beijing, China using an improved land surface temperature, Journal of Cleaner Production, 257, 120529, 10.1016/j.jclepro.2020.120529, 2020b.

McNorton, J. R., Arduini, G., Bousserez, N., Agustí-Panareda, A., Balsamo, G., Boussetta, S., Choulga, M., Hadade, I., and Hogan, R. J.: An Urban Scheme for the ECMWF Integrated Forecasting System: Single-Column and Global Offline Application, Journal of Advances in Modeling Earth Systems, 13, 10.1029/2020ms002375, 2021.

Meili, N., Paschalis, A., Manoli, G., and Fatichi, S.: Diurnal and seasonal patterns of global urban dry islands, Environmental Research Letters, 17, 054044, 10.1088/1748-9326/ac68f8, 2022.

Meili, N., Manoli, G., Burlando, P., Bou-Zeid, E., Chow, W. T. L., Coutts, A. M., Daly, E., Nice, K. A., Roth, M., Tapper, N. J., Velasco, E., Vivoni, E. R., and Fatichi, S.: An urban ecohydrological model to quantify the effect of vegetation on urban climate and hydrology (UT&C v1.0), Geoscientific Model Development, 13, 335-362, 10.5194/gmd-13-335-2020, 2020.

Meng, C.: The integrated urban land model, Journal of Advances in Modeling Earth Systems, 7, 759-773, 10.1002/2015ms000450, 2015.

Meng, F., Su, F., Li, Y., and Tong, K.: Changes in Terrestrial Water Storage During 2003–2014 and Possible Causes in Tibetan Plateau, Journal of Geophysical Research: Atmospheres, 124, 2909-2931, 10.1029/2018jd029552, 2019.

Meng, S., Xie, X., Zhu, B., and Wang, Y.: The relative contribution of vegetation greening to the hydrological cycle in the Three-North region of China: A modelling analysis, Journal of Hydrology, 591, 125689, 10.1016/j.jhydrol.2020.125689, 2020.

Mishra, V., Cherkauer, K. A., Niyogi, D., Lei, M., Pijanowski, B. C., Ray, D. K., Bowling, L. C., and Yang, G.: A regional scale assessment of land use/land cover and climatic changes on water and energy cycle in the upper Midwest United States, International Journal of Climatology, 30, 2025-2044, 2010.

Morabito, M., Crisci, A., Guerri, G., Messeri, A., Congedo, L., and Munafo, M.: Surface urban heat islands in Italian metropolitan cities: Tree cover and impervious surface influences, Science of the total environment, 751, 142334, 10.1016/j.scitotenv.2020.142334, 2021.

Mu, X., Wang, H., Zhao, Y., Liu, H., He, G., and Li, J.: Streamflow into Beijing and Its Response to Climate Change and Human Activities over the Period 1956–2016, Water, 12, 622, 10.3390/w12030622, 2020.

Nijssen, B., Schnur, R., and P. Lettenmaier, D.: Global retrospective estimation of soil moisture using the variable infiltration capacity land surface model, 1980-93, Journal of Climate, 14, 1790-1808, 10.1175/1520-0442(2001)014<1790:GREOSM>2.0.CO;2, 2001.

Oh, S.-G. and Sushama, L.: Urban-climate interactions during summer over eastern North America, Climate Dynamics, 57, 3015-3028, 10.1007/s00382-021-05852-3, 2021.

Oleson, K. W. and Feddema, J.: Parameterization and Surface Data Improvements and New Capabilities for the Community Land Model Urban (CLMU), J Adv Model Earth Syst, 12, e2018MS001586, 10.1029/2018MS001586, 2020.

Rodell, M., Houser, P. R., Jambor, U., Gottschalck, J., Mitchell, K., Meng, C.-J., Arsenault, K., Cosgrove, B., Radakovich, J., Bosilovich, M., Entin, J. K., Walker, J. P., Lohmann, D., and Toll, D.: The Global Land Data

671   Assimilation System, Bull. Amer. Meteor. Soc., 85, 381-394, https://doi.org/10.1175/BAMS-85-3-381, 2004.

672   Salvadore, E., Bronders, J., and Batelaan, O.: Hydrological modelling of urbanized catchments: A review and
673   future directions, Journal of Hydrology, 529, 62-81, 10.1016/j.jhydrol.2015.06.028, 2015.

674   Shangguan, W., Dai, Y., Liu, B., Zhu, A., Duan, Q., Wu, L., Ji, D., Ye, A., Yuan, H., Zhang, Q., Chen, D.,
675   Chen, M., Chu, J., Dou, Y., Guo, J., Li, H., Li, J., Liang, L., Liang, X., Liu, H., Liu, S., Miao, C., and Zhang, Y.: A
676   China data set of soil properties for land surface modeling, Journal of Advances in Modeling Earth Systems, 5,
677   212-224, 10.1002/jame.20026, 2013.

678   Simón-Moral, A., Dipankar, A., Roth, M., Sánchez, C., Velasco, E., and Huang, X. Y.: Application of
679   MORUSES single-layer urban canopy model in a tropical city: Results from Singapore, Quarterly Journal of the
680   Royal Meteorological Society, 146, 576-597, 10.1002/qj.3694, 2019.

681   Sun, T. and Grimmond, S.: A Python-enhanced urban land surface model SuPy (SUEWS in Python, v2019.2):
682   development, deployment and demonstration, Geoscientific Model Development, 12, 2781-2795, 10.5194/gmd-
683   12-2781-2019, 2019.

684   Wang, C., Wang, Z. H., and Yang, J.: Cooling Effect of Urban Trees on the Built Environment of Contiguous
685   United States, Earth's Future, 6, 1066-1081, 10.1029/2018ef000891, 2018.

686   Wang, Y., Xie, X., Liang, S., Zhu, B., Yao, Y., Meng, S., and Lu, C.: Quantifying the response of potential
687   flooding risk to urban growth in Beijing, Science of the total environment, 705, 135868,
688   10.1016/j.scitotenv.2019.135868, 2020.

689   Wang, Y., Xie, X., Shi, J., Zhu, B., Jiang, F., Chen, Y., and Liu, Y.: Accelerated hydrological cycle on the
690   Tibetan Plateau evidenced by ensemble modeling of Long-term water budgets, Journal of Hydrology, 615, 128710,
691   10.1016/j.jhydrol.2022.128710, 2022.

692   Xie, X., Liang, S., Yao, Y., Jia, K., Meng, S., and Li, J.: Detection and attribution of changes in hydrological
693   cycle over the Three-North region of China: Climate change versus afforestation effect, Agricultural and Forest
694   Meteorology, 203, 74-87, 10.1016/j.agrformet.2015.01.003, 2015.

695   Yang, G., Bowling, L. C., Cherkauer, K. A., Pijanowski, B. C., and Niyogi, D.: Hydroclimatic Response of
696   Watersheds to Urban Intensity: An Observational and Modeling-Based Analysis for the White River Basin, Indiana,
697   Journal of Hydrometeorology, 11, 122-138, 10.1175/2009jhm1143.1, 2010.

698   Yang, L., Ni, G., Tian, F., and Niyogi, D.: Urbanization Exacerbated Rainfall Over European Suburbs Under
699   a Warming Climate, Geophysical Research Letters, 48, 10.1029/2021gl095987, 2021.

700   Yao, R., Wang, L., Huang, X., Liu, Y., Niu, Z., Wang, S., and Wang, L.: Long-term trends of surface and
701   canopy layer urban heat island intensity in 272 cities in the mainland of China, Science of the total environment,
702   772, 145607, 10.1016/j.scitotenv.2021.145607, 2021.

703   Yousefi Sohi, H., Zahraie, B., Dolatabadi, N., and Zebarjadian, F.: Application of VIC-WUR model for
704   assessing the spatiotemporal distribution of water availability in anthropogenically-impacted basins, Journal of
705   Hydrology, 637, 131365, https://doi.org/10.1016/j.jhydrol.2024.131365, 2024.

706   Zhang, X., Zhao, X., Li, W., Liang, S., Wang, D., Liu, Q., Yao, Y., Jia, K., He, T., Jiang, B., Wei, Y., and Ma,
707   H.: An Operational Approach for Generating the Global Land Surface Downward Shortwave Radiation Product
708   From MODIS Data, IEEE Transactions on Geoscience and Remote Sensing, 57, 4636-4650,
709   10.1109/tgrs.2019.2891945, 2019.

710   Zhao, Q., Ding, Y., Wang, J., Gao, H., Zhang, S., Zhao, C., Xu, J., Han, H., and Shangguan, D.: Projecting
711   climate change impacts on hydrological processes on the Tibetan Plateau with model calibration against the glacier
712   inventory data and observed streamflow, Journal of Hydrology, 573, 60-81, 10.1016/j.jhydrol.2019.03.043, 2019.

713   Zhong, X., Wang, L., Zhou, J., Li, X., Qi, J., Song, L., and Wang, Y.: Precipitation Dominates Long-Term
714   Water Storage Changes in Nam Co Lake (Tibetan Plateau) Accompanied by Intensified Cryosphere Melts
715   Revealed by a Basin-Wide Hydrological Modelling, Remote Sensing, 12, 1926, 10.3390/rs12121926, 2020.

716   Zhou, D., Xiao, J., Bonafoni, S., Berger, C., Deilami, K., Zhou, Y., Frolking, S., Yao, R., Qiao, Z., and Sobrino,
717   J.: Satellite Remote Sensing of Surface Urban Heat Islands: Progress, Challenges, and Perspectives, Remote
718   Sensing, 11, 48, 10.3390/rs11010048, 2018.
719   Zhou, J., Li, J., and Yue, J.: Analysis of urban heat island (UHI) in the Beijing, IGARSS, 3327-3330, 2010.
720   Zhu, B., Xie, X., Meng, S., Lu, C., and Yao, Y.: Sensitivity of soil moisture to precipitation and temperature
721   over China: Present state and future projection, Science of The Total Environment, 705, 135774,
722   https://doi.org/10.1016/j.scitotenv.2019.135774, 2020.
723   Zhu, B., Xie, X., Lu, C., Lei, T., Wang, Y., Jia, K., and Yao, Y.: Extensive Evaluation of a Continental-Scale
724   High-Resolution Hydrological Model Using Remote Sensing and Ground-Based Observations, Remote Sensing,
725   13, 1247, 10.3390/rs13071247, 2021.

726